Atmos. Chem. Phys., 26, 13139–13156, 2026
https://doi.org/10.5194/acp-26-13139-2026

Atmospheric Chemistry and Physics
Open Access
EGU

Research article

Ozone downward flux revealed by high-resolution differential absorption lidar over Tibet during stratosphere-troposphere exchange

Ruichun Dong[1], **Xin Fang**[1,2], **Chengyun Yang**[1,2], **and Tao Li**[1,2]

[1]National Key Laboratory of Deep Space Exploration/School of Earth and Space Sciences, University of Science and Technology of China, Hefei, Anhui, China
[2]CAS Center for Excellence in Comparative Planetology/CAS Key Laboratory of Geospace Environment/Mengcheng National Geophysical Observatory, University of Science and Technology of China, Hefei, Anhui, China

Correspondence: Xin Fang (xinf@ustc.edu.cn)

Received: 5 June 2026 – Discussion started: 7 July 2026
Revised: 6 September 2026 – Accepted: 7 September 2026 – Published: 17 September 2026

Abstract. This study characterizes a prominent ozone intrusion event driven by stratosphere-to-troposphere exchange (STE) that occurred on 18–19 October 2017. The analysis is enabled by high spatiotemporal resolution ozone profile observations from the USTC Ozone Lidar deployed at Yangbajing, Tibet (29° N, 99° E). The high-spatiotemporal-resolution lidar observations resolve a series of short-lived, rapid ozone descent episodes during the STE event. Temperature profiles independently retrieved from the simultaneously measured 387 nm N_2 Raman signal further reveal a close temporal correspondence between these ozone descent episodes and temperature variations in the tropopause region, with temperature gradients exceeding $8\,K\,km^{-1}$ for six of the seven identified episodes. Based on Wei's flux diagnostic and a sensitivity test of PV-based dynamical tropopause thresholds, 3 PVU is adopted as the representative threshold for this event. ECMWF Reanalysis v5 (ERA5) is then used to characterize the spatiotemporal evolution of cross-tropopause mass fluxes over 25–28° N, 95–99° E, showing that the ozone variations observed by the lidar were modulated by gravity waves associated with the tropopause fold. In addition, lidar-measured ozone profiles are incorporated into a cross-tropopause ozone flux calculation framework, yielding an instantaneous peak STE ozone flux of about $3\text{–}4 \times 10^{-10}\,kg\,s^{-1}\,m^{-2}$, slightly higher than the corresponding ERA5 value, while maintaining strong agreement in overall flux magnitude and temporal evolution throughout the event. These results show that high-resolution vertical ozone observations and Raman-retrieved temperature profiles from the USTC Ozone Lidar, combined with wind field data, enable accurate quantification of STE-related ozone fluxes. This approach facilitates in-depth investigation of coupled atmospheric composition and dynamical processes.

1 Introduction

Stratosphere-Troposphere Exchange (STE) has been investigated for several decades and is recognized as a key process controlling the budgets of ozone, water vapor, and other trace constituents in the upper troposphere and lower stratosphere (UTLS) (Chen et al., 2006; Stohl et al., 2003). STE exerts a strong influence on upper-tropospheric ozone and plays an important role in the UTLS radiative budget, dynamical structure, chemical processing, and microphysical evolution (Lelieveld and Dentener, 2000). At the global scale, STE is associated with the large-scale atmospheric circulation, while individual exchange events occur over a wide range of spatial and temporal scales and are strongly modulated by synoptic-scale and mesoscale dynamical processes (Holton et al., 1995; Stohl et al., 2003). In the extratropics, tropopause folds, cutoff lows, upper-level jets, and wave-related disturbances have been identified as key mechanisms facilitating the transport of stratospheric air into the troposphere (Stohl et al., 2003). In particular, tropopause folds are closely related to upper-level frontogenesis and jet-stream dynamics and constitute an important pathway for cross-tropopause exchange. The subtropical jet is particularly relevant in this context because its strong horizontal and vertical wind shear favors tropopause deformation and folding. Global analyses by Sprenger et al. (2003) showed pronounced stratosphere-to-troposphere transport (STT) in the subtropical region and demonstrated that tropopause folds occur preferentially in the subtropics, with a substantial fraction of cross-tropopause exchange events between 20 and 40° latitude being associated with such folds. Subsequent global climatological analyses further demonstrated pronounced geographical and seasonal variations in tropopause-fold occurrence and its relationship with cross-tropopause transport (Škerlak et al., 2015).

Ozone is a particularly effective tracer for investigating Stratosphere-to-Troposphere Transport (STT) due to the strong contrast in ozone abundance between the stratosphere and troposphere. Accordingly, cross-tropopause ozone transport has been extensively studied using numerical models, satellite observations, ozonesondes, aircraft measurements, and ground-based remote sensing. For example, Olsen et al. (2004) quantified the relationship between extratropical cross-tropopause mass flux and ozone flux, demonstrating that ozone transport depends on both mass exchange and ozone concentration near the tropopause.

Internationally, a variety of observational and modeling studies have further advanced the understanding of STE structure and its fine-scale variability. High-resolution ground-based ozone lidar measurements are particularly valuable for resolving thin and rapidly evolving ozone-rich layers associated with stratospheric intrusions. Eisele et al. (1999) demonstrated that high-vertical-resolution lidar observations can capture fine structures associated with tropopause folds and stratospheric intrusion events. In addition, Kuang et al. (2012) combined ground-based ozone lidar and ozonesonde observations with meteorological and potential vorticity analyses to characterize a stratospheric intrusion associated with a cutoff cyclone and tropopause fold, highlighting the capability of integrated observational systems to diagnose STE processes. These studies collectively demonstrate that high-resolution ozone profiling is essential for resolving the fine-scale structure and temporal evolution of STE events, which are often poorly represented in satellite observations and coarse-resolution reanalysis datasets.

Despite these advances, the spatial and temporal characteristics of STE exhibit pronounced regional variability. The Tibetan Plateau lies within the subtropical latitude band and is strongly influenced by the upper-level subtropical jet, making jet-related tropopause deformation and folding particularly relevant to cross-tropopause transport over this region. Shaped by its distinctive topography and circulation systems, the Tibetan Plateau and its surrounding regions display unique patterns of atmospheric composition and dynamical structure, imparting strong regional characteristics to STE. As a result, this high-elevation domain serves as a key corridor and observational window for energy and mass exchange between the stratosphere and troposphere, with important implications for understanding coupled atmospheric processes on the global scale (Yang and Lü, 2004; Chen et al., 2010).

Given that STE is a major physical mechanism governing the distribution and variability of atmospheric trace constituents in the UTLS, extensive observational and modeling studies have been conducted over the Tibetan Plateau, with particular attention to ozone and the mechanisms shaping its distribution. For example, Zhou and Zhang (2005) used TOMS satellite data to identify a summertime minimum in total-column ozone over the Plateau, commonly referred to as the Tibetan ozone valley, and related it to atmospheric ascent over the elevated terrain. Subsequent studies further demonstrated that both thermodynamic and dynamical processes contribute to the formation and maintenance of this summertime ozone minimum (Randel and Park, 2006; Randel et al., 2010). Using TOMS observations and model simulations, Tian et al. (2008) showed that the elevated summertime tropopause over the Tibetan Plateau modifies the vertical distribution of ozone in the UTLS. In addition, based on ozonesonde observations over the northeastern Tibetan Plateau, Chen et al. (2012) identified signatures of stratospheric air intruding into the troposphere along the periphery of the upper-tropospheric anticyclone. These studies collectively demonstrate that the distinctive topography and circulation of the Tibetan Plateau exert strong influences on regional ozone distributions and STE processes.

Using a springtime tropopause-folding event over the northeastern Tibetan Plateau, Zhang et al. (2010) showed that an upper-level jet associated with an intruding low-pressure trough played an important role in driving cross-tropopause exchange, with both Troposphere-to-Stratosphere Transport (TST) and Stratosphere-to-Troposphere Transport (STT) occurring during the event evolution. Nevertheless, compared with other regions where long-term ozonesonde, aircraft, and ground-based remote sensing observations are available, high-spatiotemporal-resolution observations of STE over the Tibetan Plateau remain limited. This limitation makes it difficult to resolve short-lived and vertically confined ozone structures and to quantify their relationship with rapid dynamical and thermal variability near the tropopause.

To address this observational gap, we developed a mobile differential absorption lidar (DIAL) system (Fang et al., 2019) capable of high-spatiotemporal-resolution, long-duration profiling of ozone in both the troposphere and stratosphere. Based on measurements from this platform, we present a comprehensive analysis of an STE-related ozone descent event over Tibet. Section 2 describes the datasets used in this study, with emphasis on the mobile differential absorption ozone lidar deployed at Yangbajing, Tibet, and presents intercomparisons and accuracy validation of the retrieved ozone profiles. In Sect. 3, we corroborate the STE-related ozone descent detected by the lidar using ERA5 reanalysis fields; we then select an appropriate tropopause definition and diagnose cross-tropopause mass fluxes over the observational domain, quantifying the spatial distribution of the mass flux across the tropopause. Building on these diagnostics, we combine the lidar-measured ozone profiles with ERA5 wind fields to estimate cross-tropopause ozone fluxes, enabling a quantitative, observation-based assessment. Section 4 summarizes the main conclusions and outlines directions for future work.

2 Data sources and lidar system overview

The data used in this study were acquired with a mobile differential absorption lidar (USTC Ozone Lidar) system deployed by our group at Yangbajing, Tibet (29° N, 99° E), which enables simultaneous observations of ozone in both the troposphere and stratosphere. The complete system configuration, technical specifications and performance characterization have been described in detail by Fang et al. (2019). Here, we summarize only the key instrumental parameters directly relevant to the observations and analyses presented in this study. Satellite imagery of the lidar site in Tibet and the on-site layout of the ozone lidar system are shown in Fig. 1a and b, respectively. After performance tuning and testing in Huainan, Anhui Province, the mobile ozone lidar system was transferred to Yangbajing for routine observations beginning in October 2017. It is one of the few mobile DIAL stations worldwide capable of simultaneously profiling tropospheric and stratospheric ozone (McDermid et al., 1991; Godin-Beekmann et al., 2003; Hansen et al., 2003; Baray et al., 2013), and represents a distinctive example of such a system operating at the highest altitude among comparable platforms globally (approximately 4300 m above sea level). Ground-based ozone lidar has also been extensively applied to studies of stratosphere-to-troposphere transport (STT) and stratospheric intrusions. Previous studies have demonstrated the capability of ozone lidar to resolve ozone-rich layers associated with cross-tropopause exchange and tropopause-folding events (Ancellet et al., 1991; Eisele et al., 1999). Subsequent lidar observations have been used to investigate the descent, evolution, and mixing of stratospheric ozone intrusions in the free troposphere (Langford et al., 1996; Kuang et al., 2012). More recently, long-term ozone lidar observations have further demonstrated the frequent occurrence and substantial influence of stratospheric intrusion layers in the free troposphere (Trickl et al., 2020). These studies demonstrate the important role of high-resolution ozone lidar observations in characterizing the fine-scale structure and temporal evolution of STT.

The mobile differential absorption ozone lidar combines the differential absorption technique with distinct backscattering mechanisms. Schematics of the mobile ozone DIAL system and of the emission reception configuration for the different detection wavelengths are shown in Fig. 1c and d, respectively. Multiple wavelengths are employed to accommodate the large difference in ozone abundance between the troposphere and stratosphere and the corresponding requirements for differential-absorption sensitivity and detection range. For tropospheric ozone measurements, where ozone abundance is relatively low, the system employs the 289/299 nm DIAL pair to provide sufficient differential ozone absorption sensitivity. These two wavelengths are generated through stimulated Raman scattering by separately pumping D_2 and H_2 Raman cells with 266 nm radiation obtained from the fourth harmonic of a Nd:YAG laser, producing the first-order Stokes wavelengths near 289 and 299 nm, respectively (Papayannis et al., 1999; Kourtidis et al., 2002; Fang et al., 2019). For stratospheric ozone measurements, where ozone abundance is substantially higher, the system employs the 308/355 nm DIAL pair. The ozone-absorbing wavelength at 308 nm is directly generated by a XeCl excimer laser, whereas the reference wavelength at 355 nm is generated through third-harmonic generation of the 1064 nm fundamental output of a Nd:YAG laser. This 308/355 nm configuration has been widely employed in stratospheric ozone DIAL systems (McDermid et al., 1991; Godin-Beekmann et al., 2003; Fang et al., 2019). In addition to the elastic backscatter signals at the transmitted wavelengths, N_2 vibrational Raman returns at 332 and 387 nm, corresponding to excitation at 308 and 355 nm, respectively, are simultaneously detected (McGee et al., 1993). These Raman channels provide additional information for reducing aerosol/backscatter-related effects on the ozone retrieval. In the receiver subsystem, four independent telescopes, each with a 1.25 m aperture, are combined into a collecting array with an effective diameter exceeding 2.2 m to detect signals at 308, 332, 355, and 387 nm, enabling ozone measurements from the tropopause to the upper stratosphere over an altitude range of 18–50 km. This array-based design enhances the signal-to-noise ratio for stratospheric observations. A separate 1 m aperture prime-focus telescope receives the 289 and 299 nm signals for ozone detection over 8–19 km above ground level (km a.g.l.), while two 0.21 m aperture Newtonian telescopes receive the same wavelengths for measurements over 5–10 km a.g.l., thereby extending coverage from the troposphere to the lower stratosphere across 5–19 km a.g.l. Together, the seven telescopes provide simultaneous ozone profiling from 5 to 50 km a.g.l., spanning both the troposphere and stratosphere.

To ensure accurate ozone measurements, the laser beam axis must be properly aligned with the receiving telescope, and the telescope field of view must adequately overlap with the laser emission field. As shown in Fig. 1c, a mechanical chopper was placed in the optical path to reduce noise from strong near-field backscatter. In routine operation, the system records raw signal files at a 1 min output interval,

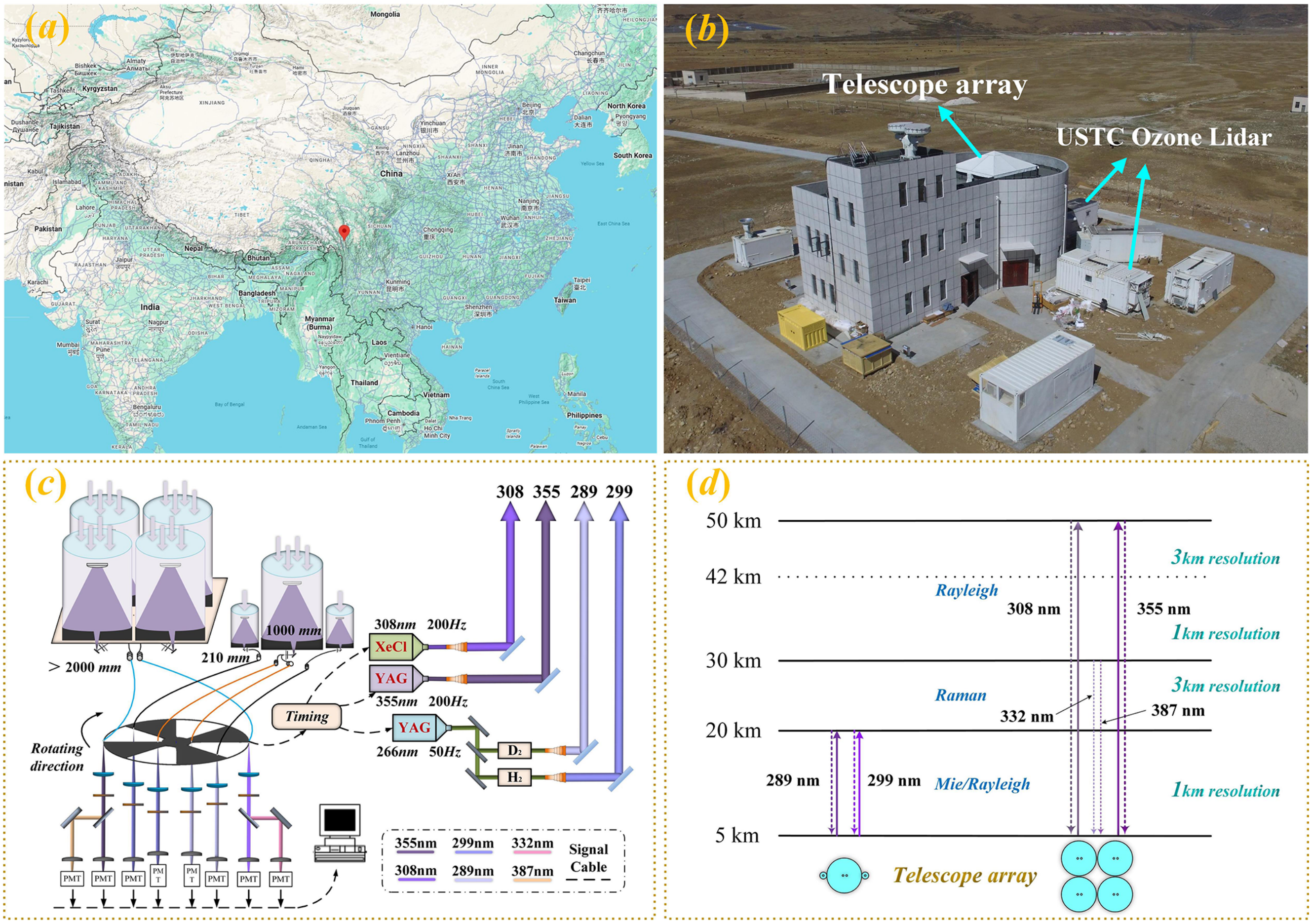

Figure 1. **(a)** Satellite image of the radar observation site on the Tibetan Plateau (Map data © Google Earth 2026); **(b)** field layout of the ozone lidar system; **(c)** schematic of the mobile ozone lidar system; **(d)** altitude ranges corresponding to different laser emission wavelengths.

with a vertical bin size of 61.44 m and 2048 range bins. For stratospheric ozone retrieval, the 1 min photon-counting signals are accumulated to achieve an effective integration time of 30 min, thereby ensuring sufficient signal quality in the stratosphere. After saturation correction, the resulting wavelength-dependent photon-count profiles and signal-to-noise ratios are shown in Fig. 2a–d. As shown in Fig. 2, the SNR is sufficient across the altitude ranges corresponding to the different wavelengths presented in Fig. 1c and d.

Background noise, averaged over the altitude range of 115–125 km, was subtracted from the raw signals. After denoising the raw backscattered optical signals using wavelet-transform-based signal processing (Fang and Huang, 2004; Yin and Wang, 2006; Boggess and Narcowich, 2009), ozone number-density profiles were retrieved using the differential absorption lidar (DIAL) equation (Kovalev and Eichinger, 2004). The retrieval considers several important factors affecting the retrieved ozone number density, including the temperature dependence of the ozone absorption cross-sections, absorption by interfering atmospheric species, and wavelength-dependent molecular and aerosol backscatter and extinction (Gimmestad, 2005). Aerosols and clouds represent additional sources of uncertainty in ozone DIAL measurements. Differences in aerosol backscatter and extinction between the online and offline wavelengths can introduce systematic errors, particularly in the presence of strong vertical gradients in aerosol loading (Browell et al., 1985; Kovalev and Bristow, 1996). Additional wavelength and Raman measurements can help constrain these aerosol-related contributions. In the USTC Ozone Lidar, the N_2 vibrational Raman returns at 332 and 387 nm provide complementary information for reducing aerosol/backscatter-related effects in the upper-tropospheric and stratospheric ozone retrievals. The retrieved ozone profiles are further evaluated in the present study through comparisons with ERA5 and independent Aura satellite observations, as shown in Fig. 3.

The ozone number density profiles retrieved from the lidar observations over five altitude intervals are shown in Fig. 3a. Because differences in detection wavelength, laser pulse energy, and telescope field of view determine the effective retrieval range for each channel, the five profile segments were merged using 3-bin overlap regions to produce a continu-

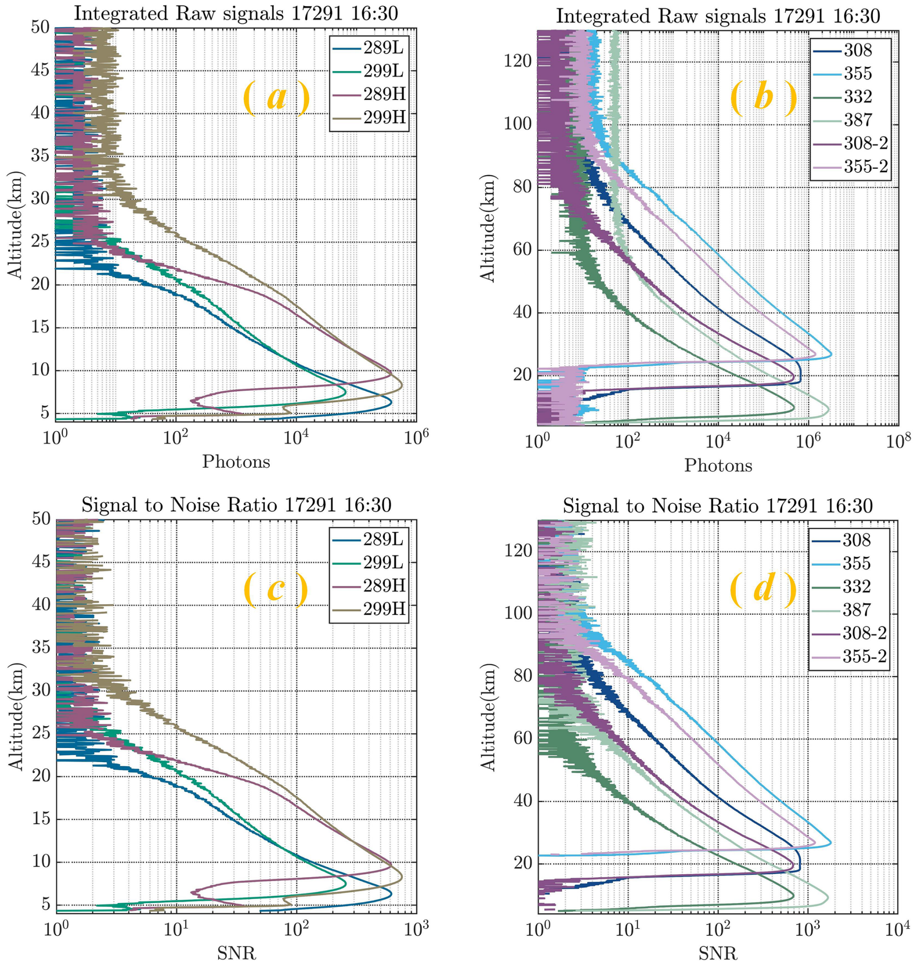

Figure 2. Wavelength-dependent photon returns and corresponding signal-to-noise ratios for the mobile ozone DIAL system (USTC Ozone Lidar).

ous ozone profile. The merged profile was then compared with ERA5 data at the corresponding time, and further cross-validated against observations from the Ozone Monitoring Instrument (OMI; Liu et al., 2010) and the Microwave Limb Sounder (MLS; Waters et al., 2006) aboard the Aura satellite (Schoeberl et al., 2006), as shown in Fig. 3b.

The results show that the ozone profile retrieved from USTC Ozone Lidar agrees well overall with ERA5. It should be noted, however, that satellite observations are constrained by orbital sampling and overpass timing. On this day, the MLS overpass occurred at 18:50 UT at 25.22° N, 105.20° E. Below 25 km, the observed ozone concentrations were broadly consistent with the USTC Ozone Lidar measurements, whereas above 25 km, MLS showed systematically higher ozone concentrations at the same altitudes. This discrepancy is likely related to the large spatial separation between the satellite overpass location and the lidar site. By contrast, the OMI overpass occurred at 07:10 UT at 27.07° N, 99.34° E. Above 25 km, the ozone concentrations agreed well with the USTC Ozone Lidar retrievals, whereas below 25 km, OMI exhibited a certain positive bias relative to the lidar measurements. Although the spatial distance between the satellite footprint and the lidar station was minimized, the relatively long temporal separation between the OMI overpass and the lidar observations at the same location may still have introduced appreciable differences in ozone concentration. Overall, the ozone profiles retrieved from the USTC Ozone Lidar exhibit good consistency in their overall trends with ERA5, with the two datasets providing robust and complementary constraints. Moreover, the high spatial and temporal resolution of the lidar allows it to resolve fine-scale structures that are often missed by other datasets, since satellite profile data typically contain only about a dozen vertical points and ERA5 records only slightly more than 30 levels. In particular, the lidar observations resolve short-lived ozone descent structures occurring on sub-hourly to 1–2 h timescales, as discussed in Sect. 3.1. This capability is particularly valuable for detecting and analyzing short-lived but dynamically intense cross-tropopause ozone transport events.

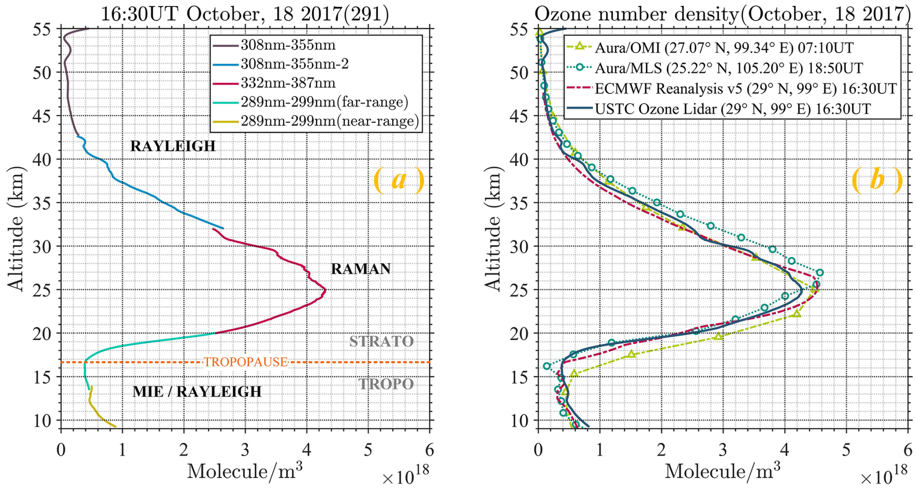

Figure 3. **(a)** Retrieved ozone concentration profiles from the ozone lidar over different altitude ranges; **(b)** comparison of the merged ozone profile with ERA5 reanalysis and Aura/OMI and Aura/MLS satellite observations. The labels "MIE/RAYLEIGH," "RAYLEIGH," and "RAMAN" in panel **(a)** indicate the different backscatter signals used for ozone retrieval: MIE/RAYLEIGH denotes the elastic Mie and Rayleigh backscatter signals at 289 and 299 nm used for tropospheric ozone retrievals; RAYLEIGH denotes the elastic Rayleigh backscatter signals at 308 and 355 nm used for stratospheric ozone retrievals; and RAMAN denotes the N_2 vibrational Raman backscatter signals at 332 and 387 nm, corresponding to excitation at 308 and 355 nm, respectively.

3 Methods and Results

3.1 Lidar observations and supporting evidence for a STE-related ozone descent event

The USTC Ozone Lidar deployed at Yangbajing, Tibet (29° N, 99° E) was developed in-house by the University of Science and Technology of China. The system enables simultaneous profiling of ozone in the troposphere and stratosphere with high spatial and temporal resolution, providing a particularly valuable observational constraint on ozone variability over the Tibetan Plateau, where in situ data remain sparse. The lidar retrievals also allow us to identify clear signatures of downward ozone transport. Influenced by its unique high elevation topography and the Asian monsoon, the Tibetan Plateau is recognized as one of the most active regions for Stratosphere-Troposphere Exchange (STE) (Chen et al., 2006). Under these conditions, ozone transport from the stratosphere across the tropopause is likely to be an important source of background tropospheric ozone over Tibet, with potential implications for regional climate regulation and for the global coupling of chemistry and climate (Gettelman et al., 2002; Duan and Wu, 2005). In this section, we use ERA5 global reanalysis fields (0.25° × 0.25° spatial resolution; 1 h temporal resolution) as supporting evidence to analyze the STE event captured by the ozone-profiling lidar and to provide an initial observational assessment of its evolution.

As shown in Fig. 4, the USTC Ozone Lidar captures pronounced temporal variations in the vertical distribution of ozone near the tropopause during the nights of 18 and 19 October 2017. To ensure an adequate signal-to-noise ratio, photon-counting returns were accumulated over 30 min and processed using a moving time-window method (Duchnowski and Wyszkowska, 2025), yielding a continuous ozone concentration distribution as a function of height and time. It is worth noting that ozone DIAL measurements are conducted only at night and are limited by weather conditions. As a result, the ozone results typically appear as banded segments separated by temporal gaps, shown in Fig. 4. Figure 4a shows the evolution observed during 16:00–21:00 UT on 18 October. An ozone-enhanced layer exhibits a pronounced downward displacement in the time–height cross-section, forming the tilted structure indicated by the blue arrow. Figure 4b shows the subsequent evolution during 15:00–21:00 UT on 19 October, when the ozone-enhanced structure exhibits an overall upward displacement, as indicated by the orange arrow. At this stage of the analysis, these features are interpreted descriptively as vertical displacements of ozone-rich structures near the tropopause; whether they represent irreversible cross-tropopause transport or primarily reflect tropopause displacement is examined using the dynamical and flux diagnostics presented below.

Within these broader variations, the lidar resolves several short-lived episodes of downward displacement of ozone-enhanced structures, marked T0–T6 in Fig. 4. Some episodes persist for 1–2 h, whereas others last for less than 1 h. Their short duration highlights the capability of the lidar to resolve rapid variability in ozone structure near the tropopause that may not be captured by satellite observations or lower-resolution meteorological datasets. Previous studies have given comparatively limited attention to such short-lived ozone structures near the tropopause. Importantly, these fea-

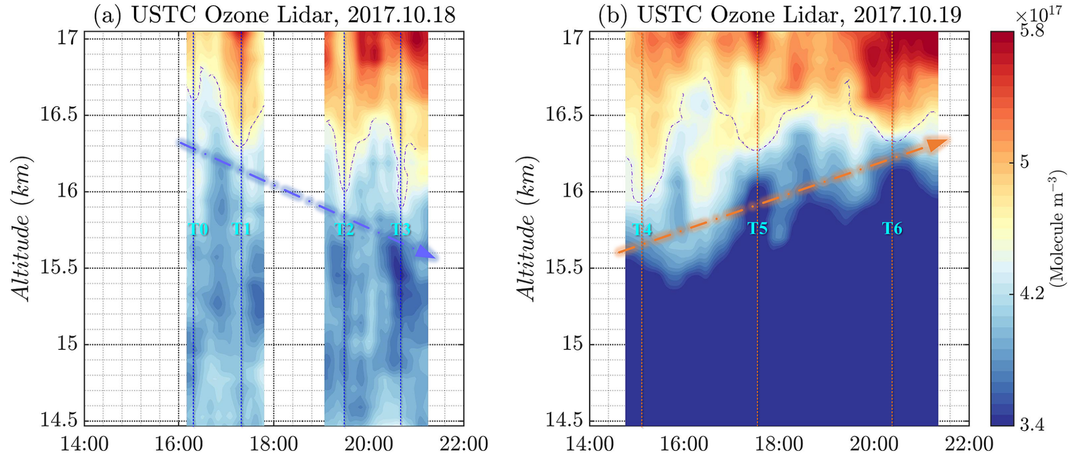

Figure 4. Temporal evolution of the ozone distribution near the tropopause observed by the USTC Ozone Lidar on **(a)** 18 October and **(b)** 19 October 2017. The blue arrow in **(a)** indicates the downward displacement of the ozone-enhanced structure, whereas the orange arrow in **(b)** indicates its overall upward displacement during the subsequent evolution. T0–T6 mark the short-lived downward-displacement episodes discussed in the text.

tures should not necessarily be interpreted as individual cross-tropopause transport events, since rapid tropopause oscillations or undulations may also produce apparent vertical displacements of ozone-rich layers. Their repeated occurrence on sub-hourly to hourly timescales nevertheless provides a useful observational perspective on fine-scale ozone variability and tropopause dynamics. The relationship of these features to tropopause variability and cross-tropopause transport is examined further using the temperature, dynamical, and flux diagnostics presented below.

To corroborate the suspected STE-related ozone descent observed by the ozone lidar in autumn 2017, we further use ERA5 global reanalysis fields as an independent line of evidence. A prerequisite for diagnosing cross-tropopause exchange during STE events is a robust identification of the tropopause. For an initial ERA5-based screening of the event (interpolate the ERA5 data at uniform intervals of 0.5 hPa), the tropopause height is determined using the thermodynamic definition. Following the World Meteorological Organization (WMO) lapse-rate criterion proposed in 1986 (Wei, 1987), the thermodynamic tropopause is defined as the lowest level above the 500 hPa surface at which the atmospheric temperature lapse rate decreases to $2\,^{\circ}\mathrm{C\,km^{-1}}$ or less, provided that the mean lapse rate within the 2 km layer above this level does not exceed $2\,^{\circ}\mathrm{C\,km^{-1}}$. In this study, the thermodynamic tropopause was determined independently at each available ERA5 time step. Specifically, the temperature lapse rate was calculated from the corresponding ERA5 vertical temperature profile, and the WMO lapse-rate criterion was then applied to identify the tropopause. Thus, both the temperature lapse rate and the resulting tropopause height were allowed to vary with time. Analysis of ERA5 data during the periods covered by USTC Ozone Lidar observations reveals a pronounced cross-tropopause ozone descent event. We therefore focus on ERA5 data at the Yangbajing site for 16–19 October 2017. The continuous temporal coverage provided by ERA5 during this period allows the evolution of the event to be captured more completely, as illustrated in Fig. 5a. A strong STE-related ozone descent is evident during 18–19 October 2017, in close agreement with the USTC Ozone Lidar observations.

Both the USTC Ozone Lidar observations and ERA5 capture the onset and recovery phases of this ozone descent event. Differences between the lidar-retrieved ozone concentrations and those from ERA5 are further quantified. As shown in Fig. 5b, the ozone number density variations observed by the USTC Ozone Lidar during the STE event are compared with the corresponding ERA5 values. To ensure a consistent comparison, the analysis is performed at the tropopause level (16.6 km), and the 95 % confidence interval of the lidar retrievals is also shown. Notably, ERA5 provides hourly-resolution data, whereas the ozone lidar yields full-profile ozone measurements with 1 min update intervals. Figure 5b shows that the tropopause-level (16.6 km) ozone number densities measured by the USTC Ozone Lidar during 18–19 October 2017 agree closely with ERA5 in both absolute magnitude and temporal evolution. However, comparing Fig. 5a with Fig. 4b indicates that during the recovery phase on 19 October 2017, the ozone number densities retrieved by USTC Ozone Lidar below 15.5 km are systematically slightly lower than those in ERA5. Given the high SNR of the lidar returns during this period, the discrepancy is more likely to reflect a modest overestimation by ERA5 of the ozone number density associated with stratosphere-to-troposphere transport at this stage.

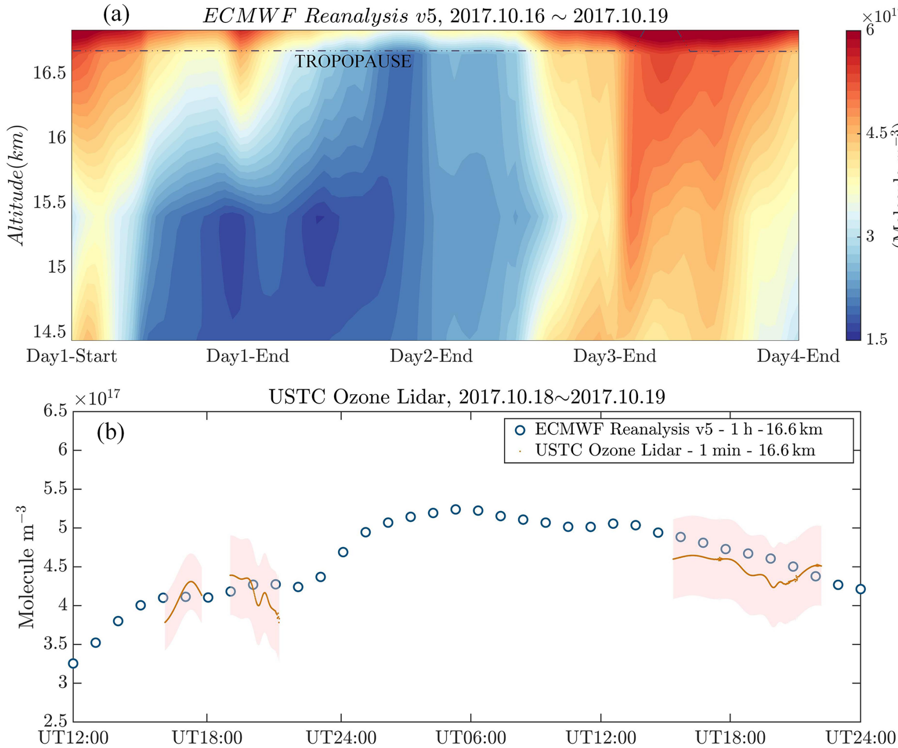

Figure 5. **(a)** ERA5 depiction of the STE evolution near the tropopause over Yangbajing during 16–19 October 2017; **(b)** comparison of lidar-observed and ERA5 ozone concentrations at the tropopause level (16.6 km) during 18–19 October 2017.

3.2 Tropopause definition and cross-tropopause flux diagnostics

Mass and trace-constituent exchange between the stratosphere and troposphere is a central component of the coupled troposphere–stratosphere system. In 1987, Wei proposed a diagnostic framework for quantifying this exchange, in which all physical processes contributing to cross-tropopause transport can be expressed in an explicit mathematical form (Reiter, 1975; Wirth and Egger, 1999). The general form can be written as:

$$F(f) = \left[\rho J_\eta f \left(\frac{\mathrm{d}\eta}{\mathrm{d}t} - \frac{\partial \eta}{\partial t_{z_0}} - \boldsymbol{U} \cdot \nabla_{z_0} \eta\right)\right]_{\eta_B}, \quad (1)$$

where $F(f)$ is the air mass flux across the tropopause, ρ is the air density near the tropopause, η is a generalized vertical coordinate, $J_\eta = \partial z / \partial \eta$ is the vertical coordinate-transformation factor between the generalized vertical coordinate η and geometric height z, z_0 denotes the tropopause, $\mathrm{d}\eta/\mathrm{d}t$ is the vertical velocity in η coordinates, $\boldsymbol{U}$ is the horizontal wind vector, and f is the constituent mixing ratio. In pressure coordinates, this expression becomes:

$$F(\rho) = -g^{-1} \left(w - \boldsymbol{U} \cdot \nabla_{z_0} p - \frac{\partial p}{\partial t_{z_0}}\right). \quad (2)$$

A key advantage of Wei's diagnostic formulation is that it allows the upward and downward cross-boundary fluxes to be computed separately and can be applied to any atmospheric constituent across an arbitrary reference surface. Given the large contrast in ozone mass mixing ratios between the stratosphere and troposphere, and the common assumption that an air mass becomes well mixed over a relatively short timescale after crossing the tropopause, quantitative assessments based on ozone profiles require the upward and downward fluxes to be treated separately. As noted above, we initially located the thermodynamic tropopause using changes in the vertical temperature lapse rate. In some situations, however, particularly near jet streams, this tropopause can be poorly defined. Because the following analysis examines lidar observations in detail and because the Yangbajing site lies in the low-to-mid latitudes, where large-scale dynamics and strong disturbances can substantially perturb the thermal structure, defining the tropopause solely from lapse-rate criteria may introduce appreciable uncertainty.

Holton noted that the tropopause is better regarded as a quasi-material surface (Holton et al., 1995). This perspective is well captured by the dynamical tropopause defined in terms of potential vorticity (PV), and cross-tropopause transport studies therefore commonly adopt a PV-based tropopause, typically using thresholds in the range of 1.5–4 PVU (where PVU denotes the potential vorticity unit). Moreover, Yang et al. showed that the choice of PV threshold can substantially affect estimates of cross-tropopause exchange, and advocated selecting an optimal threshold based

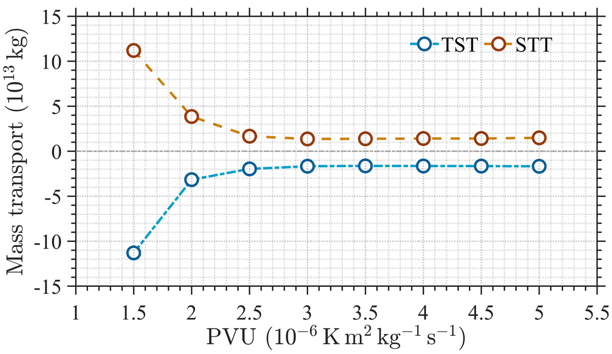

Figure 6. Transport sensitivity to PVU threshold during 18–19 October 2017.

on its correlation with observations or diagnostic quantities (Yang and Lü, 2003). It should be noted that the PV fields used here are derived from ERA5 and therefore cannot be expected to reproduce the fine-scale structures resolved by the lidar on a point-by-point or event-by-event basis. In this study, the ERA5-derived PV is used primarily to characterize the regional dynamical tropopause and the larger-scale dynamical environment associated with the STE event, rather than to reproduce the individual short-lived ozone features observed by the lidar. The two datasets are therefore regarded as complementary: the lidar provides high-spatiotemporal-resolution information on local ozone variability, whereas ERA5 provides the dynamically consistent three-dimensional meteorological fields required for diagnosing the tropopause structure and cross-tropopause transport.

Following the approach of Yang et al., we conduct a sensitivity analysis over a domain centered on the Yangbajing ozone lidar site (29° N, 99° E), spanning 25–32° N and 94–104° E, to assess how the choice of PV threshold influences the diagnosed cross-tropopause flux. As shown in Fig. 6, we quantify the changes in cross-tropopause transport on 18–19 October 2017 associated with different PV thresholds within this region. The results indicate that the estimated cross-tropopause flux is highly sensitive to the choice of threshold. For PV thresholds below 3 PVU, both upward and downward transports are relatively large, exhibiting more tropospheric characteristics; for thresholds above 3 PVU, both transports are markedly smaller, consistent with more stratospheric behavior. With increasing PV threshold, the total exchange in both troposphere-to-stratosphere transport (TST) and stratosphere-to-troposphere transport (STT) decreases. In addition, the magnitudes and temporal evolution of TST and STT suggest that, before and after the onset and recovery of the descent event on 18–19 October 2017, the total cross-tropopause transport over the study region is broadly consistent with mass conservation.

Furthermore, as shown in Fig. 7a and b, to ensure spatial continuity and robustness of the tropopause definition, we construct two PVU cross-sections from ERA5 in the vicinity of the lidar site: a zonal section along 90–110° E and a meridional section along 24–34° N. These sections show that, in some areas, tropopauses defined using lower PVU thresholds become discontinuous in pressure coordinates. By contrast, the continuity and stability improve markedly for thresholds of 2 PVU and above. Combining the sensitivity results with the cross-section structures, we consider 3 PVU ($1\,\text{PVU} = 10^{-6}\,\text{m}^2\,\text{s}^{-1}\,\text{kg}^{-1}$) to be a reasonable dynamical tropopause threshold for this event (highlighted with an orange line in Fig. 7a and b). It should be noted that the 3 PVU surface is not assumed to represent an exact tropopause height with a prescribed absolute accuracy. Rather, uncertainty associated with the dynamical tropopause definition is evaluated through the PV-threshold sensitivity analysis described above. The 3 PVU threshold is therefore adopted as a physically reasonable regional-scale dynamical boundary for this event based on both the sensitivity of the diagnosed transport and the spatial continuity of the corresponding PV surface.

Figure 7c and d shows the time evolution of the domain mean transport components over 18–19 October 2017, diagnosed from ERA5. The wind fields used in this analysis are obtained from the ERA5 reanalysis, which assimilates a wide range of atmospheric observations and provides observation-constrained, dynamically consistent three-dimensional meteorological fields (Hersbach et al., 2020). Here, the ERA5 wind fields are used to characterize the regional-scale circulation and to provide the dynamical quantities required for the cross-tropopause flux diagnosis, rather than to reproduce the individual short-lived structures resolved by the lidar. The vertical wind contribution remains relatively steady over the two days. The horizontal wind contribution is of comparable magnitude but opposite sign, so that the net flux is controlled to a large extent by variations in the tropopause. It should be stressed that tropopause undulations mainly modify the geometric boundary used in the flux diagnosis and do not, by themselves, generate strong and persistent local transport.

Given the observed tropopause variations, a natural question is whether they were driven by temperature fluctuations in the tropopause region, and in particular whether such temperature changes corresponded to the short-lived, rapid ozone descent events shown in Fig. 4. As discussed above, ERA5 is used here to characterize the larger-scale dynamical evolution of the event, but its hourly output cannot fully resolve the short-lived variability observed by the lidar. Therefore, to examine whether the individual ozone-displacement episodes are accompanied by rapid temperature variations near the tropopause, we use the higher-temporal-resolution temperature profiles retrieved from the 387 nm N_2 Raman lidar signal. As described in Sect. 2, the USTC Ozone Lidar also recorded the N_2 vibrational Raman backscatter signals at 332 and 387 nm, corresponding to the 308 and 355 nm emission wavelengths, respectively, and these signals exhibit sufficient signal-to-noise ratio over the 14 to 30 km altitude

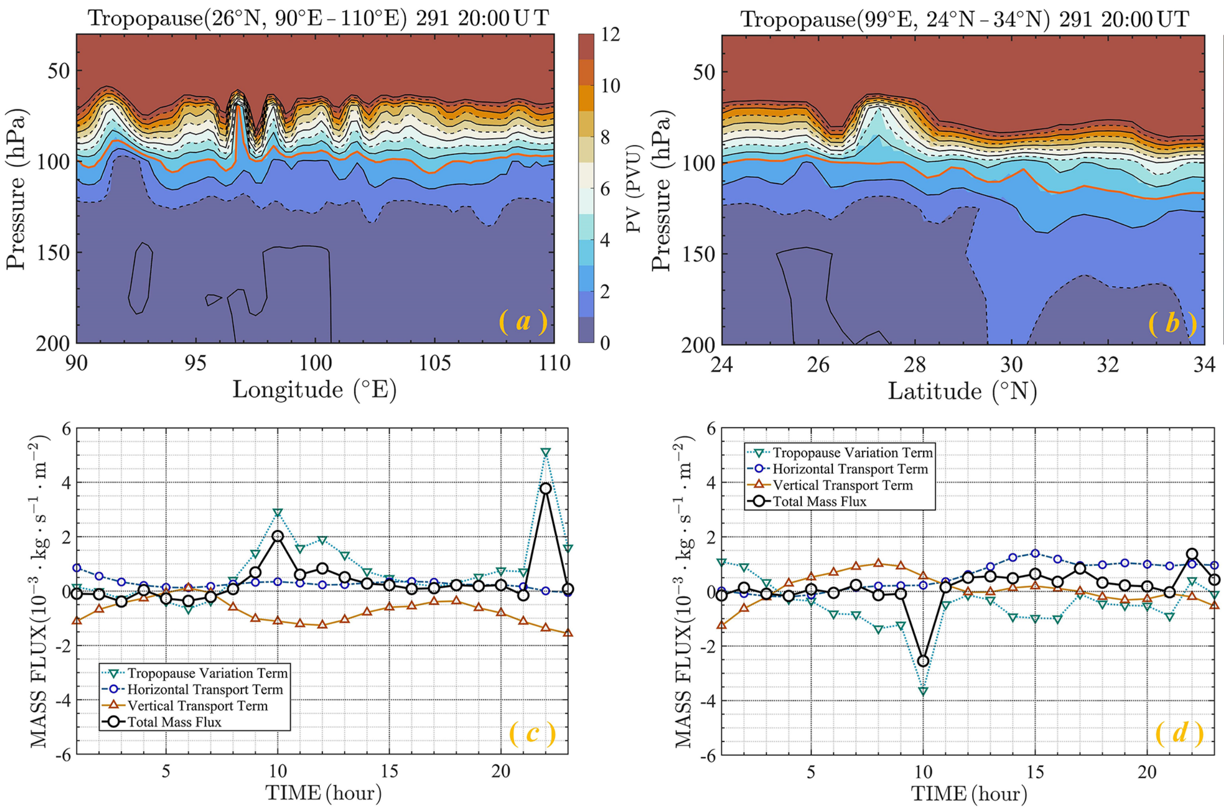

Figure 7. Potential-vorticity structure and cross-tropopause transport over the Tibetan Plateau during 18–19 October 2017. **(a)** Zonal potential-vorticity cross-section over the Tibetan Plateau region; **(b)** meridional potential-vorticity cross-section over the Tibetan Plateau region; **(c)** time evolution of the domain-mean transport components on 18 October; and **(d)** time evolution of the domain-mean transport components on 19 October.

range, as shown in Fig. 8a. Because 332 nm remains within the ozone absorption band, the 387 nm Raman signal was used to retrieve the temperature profiles. The temperature retrieval, shown in Fig. 8b, was initialized at 50 km using the temperature from the U.S. Standard Atmosphere 1976 as the upper-boundary reference (Standard, U.S., 1976), and the temperature profile was subsequently retrieved downward from this reference altitude. Comparison with ERA5 at the same times shows that the two temperature profiles are in close agreement. Figure 8c and d present the temperature variations retrieved from the 387 nm return over 14.5 to 17 km, where the temperature enhancements at the seven times T0 to T6 correspond closely to those identified in Fig. 4. These results indicate a strong association between the short-lived, rapid ozone descent events and temperature fluctuations in the tropopause region. Moreover, except for T2, all six of the other descent episodes are associated with temperature gradients exceeding 8 K km^{-1}, while T2 still exhibits a pronounced gradient of 4.2 K km^{-1}. They also represent the first detection of these descent features by the USTC Ozone Lidar, together with the first identification of their relationship to tropopause-region temperature variability using lidar-derived temperature profiles.

Turning back to Fig. 7c and d, the temporal evolution of the domain-mean flux reveals pronounced stratosphere-to-troposphere transport from 08:00 to 15:00 UT on 18 October and from 21:00 UT on 18 October to 03:00 UT on 19 October. As the analysis here focuses on the descent event, STT is defined as positive flux. The STE signal begins to recover around 10:00 UT on 19 October, consistent with the features in Fig. 5a, indicating that the dominant impact of this event is confined to within roughly 24 h. We also note that, in a domain-mean sense, the onset of the descent signal on 18 October precedes the STE timing inferred at the Yangbajing site (29° N, 99° E) from both the lidar observations and the ERA5-based diagnosis. This apparent lead suggests that the event may have first intensified in a core region away from the site, and then expanded to influence the vicinity of the observation station. To identify the main source region of the event and investigate its dynamical drivers, we further examine the spatial distribution of the cross-tropopause mass flux.

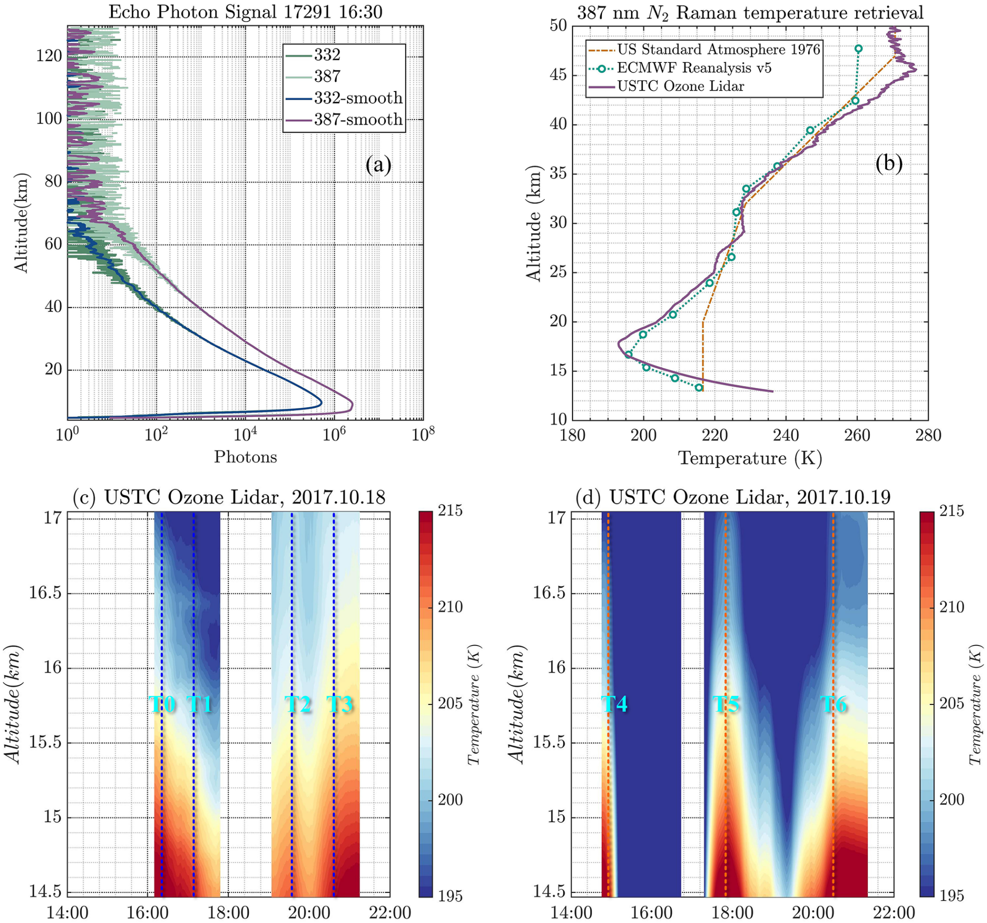

Figure 8. **(a)** 332 and 387 nm echo optical signals received by USTC Ozone Lidar and data smoothing processing; **(b)** using the USSA1976 model at a reference point of 50 km, the temperature profile obtained by inversion using the 387 nm vibrational Raman signal is compared with that of ERA5; **(c)** temperature changes obtained from the inversion on 18 October 2017; **(d)** temperature changes obtained from the inversion on 19 October 2017.

3.3 Spatial Distribution of Mass Fluxes Through the Tropopause

Using Wei's diagnostic framework together with ERA5 meteorological fields, we quantify the cross-tropopause mass exchange flux during 13:00–18:00 UT on 18 October. The flux is decomposed into contributions associated with tropopause motion, horizontal advection, and vertical motion, and we map the 6 h mean of the instantaneous mass flux over this period (Fig. 9). The red hexagon marks the location of the Yangbajing ozone lidar site. As shown in Fig. 9, the horizontal transport term exhibits a spatial distribution highly consistent with that of the total flux, with a comparable magnitude. This suggests that the spatial structure of the flux during this STE event was controlled mainly by horizontal transport. However, the flux estimates shown earlier in Fig. 7a and b indicate that the actual downward mass transport was induced by the tropopause motion term. Moreover, Fig. 9c further indicates that downward transport associated with the vertical transport term was also present at the Yangbajing lidar site. This behavior is consistent with the dynamical picture of tropopause folding (Sprenger et al., 2003; Škerlak et al., 2015). The regional PV structure indicates a tropopause-folding system over approximately 25–28° N, 95–99° E, characterized by a pronounced deformation and downward intrusion of stratospheric high-PV air toward the troposphere. The corresponding structure can also be identified in the PV cross-section near 26° N in Fig. 7a, and its spatial extent closely overlaps the region of enhanced cross-tropopause mass flux shown in Fig. 9. We note that the shorter-timescale oscillations of the tropopause observed during the evolution of the event do not contradict this regional folding interpretation. Tropopause folds developing in strongly sheared jet–front environments can be accompanied by inertia-gravity waves, wave breaking, and related instabilities, which further modulate and locally deform the tropopause and can contribute to irreversible mixing and STE (Cho et al., 1999; Bertin et al., 2001; Stohl et al., 2003). We therefore interpret the observed evolution as a regional tropopause-folding system accompanied and modulated by shorter-timescale wave-related tropopause variability.

As shown in Fig. 10, we use ERA5 meteorological fields together with Wei's diagnostic to derive the spatiotemporal evolution of cross-tropopause mass flux over the study region during 18–19 October 2017. Eulerian diagnostics formulated in pressure coordinates can be affected by numerical cancellation among individually large terms, potentially introducing substantial uncertainty into estimates of cross-tropopause fluxes (Wirth, 1995; Wirth and Egger, 1999). Lagrangian approaches, such as those developed and applied in previous studies (Wernli and Bourqui, 2002; Škerlak et al., 2014), provide an alternative that is generally less susceptible to this numerical-cancellation problem, particularly for global or large-domain analyses. However, because the present study focuses on the regional evolution of a specific STE event rather than on global-scale transport, we retained Wei's diagnostic framework but reformulated it in potential-vorticity (PV) coordinates. The corresponding results are presented in Fig. 10. Although this coordinate transformation does not eliminate all sources of uncertainty, it alleviates the numerical sensitivity and reduces part of the noise associated with cancellation among large terms. Each panel presents the 6 h mean of the instantaneous mass flux for the corresponding interval. From Fig. 10a–e, the tropopause-folding structure over 25–28° N, 95–99° E evolves markedly with time, and the associated mass flux field exhibits pronounced temporal non-stationarity and spatial heterogeneity. This sector lies along the southeastern flank of the Tibetan Plateau, within the transition zone between the entrance and exit regions of the upper-tropospheric jet, where strong shear and dynamical disturbances favor tropopause deformation, folding, and associated wave activity. Notably, the clearly identifiable folding band transitions from an approximately quasi-parallel, banded morphology in Fig. 10a and b to a meridionally offset, interleaving structure in Fig. 10g and h, suggesting a shift in the folding process from a stage modulated by near-linear wave perturbations towards a more strongly nonlinear breaking regime, possibly associated with inertial gravity waves induced by tropopause folding and their subsequent breaking. Given the fixed station location, the lidar measurements do not continuously sample the core of the tropopause fold, but more often reflect the downstream evolution and lateral modulation of the folding system (Shangguan et al., 2019; Zhang et al., 2024).

We offer the following conceptual interpretation of the dynamics. During the phase in Fig. 10a and b, PV anomalies near the tropopause are characterized by quasi-parallel PV contours, a relatively weak meridional gradient, and limited vertical extension. This structure suggests that folding is primarily modulated by disturbances, such as planetary waves and inertial gravity waves, superimposed on the shear environment of the upper-tropospheric jet (McIntyre and Palmer, 1983). In this stage, the lidar site (29° N, 99° E) lies on the northern flank of the folding band, within a wave-dominated sector that mainly reflects perturbations associated with tropopause undulations and PV field oscillations, while the net cross-tropopause transport remains limited. In Fig. 10c–f, as instability strengthens in the jet-exit region, the PV gradient across the folding band sharpens markedly. An ascending branch develops on the southern side of the fold, whereas a quasi-stationary descending branch forms on the northern side near the lidar site. The site then becomes intermittently aligned with the downstream transport pathway of the PV anomaly, indicating a transition from a fold evident in morphology to one that enables effective transport (Sprenger et al., 2003). In Fig. 10g and h, the fold exhibits clear PV tongue breakup and meridional displacement. The sawtooth-like offsets likely reflect wave breaking or nonlinear PV mixing (McIntyre and Palmer, 1983, 1984). At this stage, ascent-descent dipoles occur more frequently on smaller spatial scales, and the vertical circulation becomes shorter-lived and more localized. The previously coherent descending conduit weakens and becomes increasingly intermittent (Stohl et al., 2003). In the vicinity of the site, this fragmented circulation and enhanced mixing reduce sustained stratosphere-to-troposphere transport (STT), manifesting as a weakened or discontinuous downward flux. In addition, the ascending branch structure to the south of the site can further interrupt the local descent pathway.

Taken together, these results indicate that the short-lived, rapid ozone descent observed during this STE event was associated not only with temperature variations, but also that the onset and recovery of the event as a whole were modulated by tropopause folding and gravity waves over the region 25–28° N, 95–99° E.

3.4 Cross-tropopause ozone flux estimation based on lidar observations

Building on the mass-flux diagnostics, we further estimate the cross-tropopause ozone flux by incorporating ozone profiles from the USTC Ozone Lidar. Specifically, we use the lidar-retrieved vertical profiles of ozone number density to characterize ozone abundance in the troposphere and stratosphere and, in combination with the diagnosed cross-tropopause mass flux, to quantify ozone exchange across a layer extending several kilometers above and below the tropopause.

To ensure the robustness of the calculation, we assume that the ozone number densities measured at the lidar site (29° N, 99° E) are representative of the mean ozone level within 28.75–29.25° N and 98.75–99.25° E. Consistently, the mass flux is diagnosed from ERA5 gridded fields over the same spatial domain. Following Cui et al. (2004), the lidar-derived, vertically varying ozone mixing-ratio profiles are integrated over the 3 km layers immediately below and above the tropopause to obtain representative layer-mean mixing ratios. Consequently, the measured vertical ozone gradients within these layers are retained in the calculation rather than

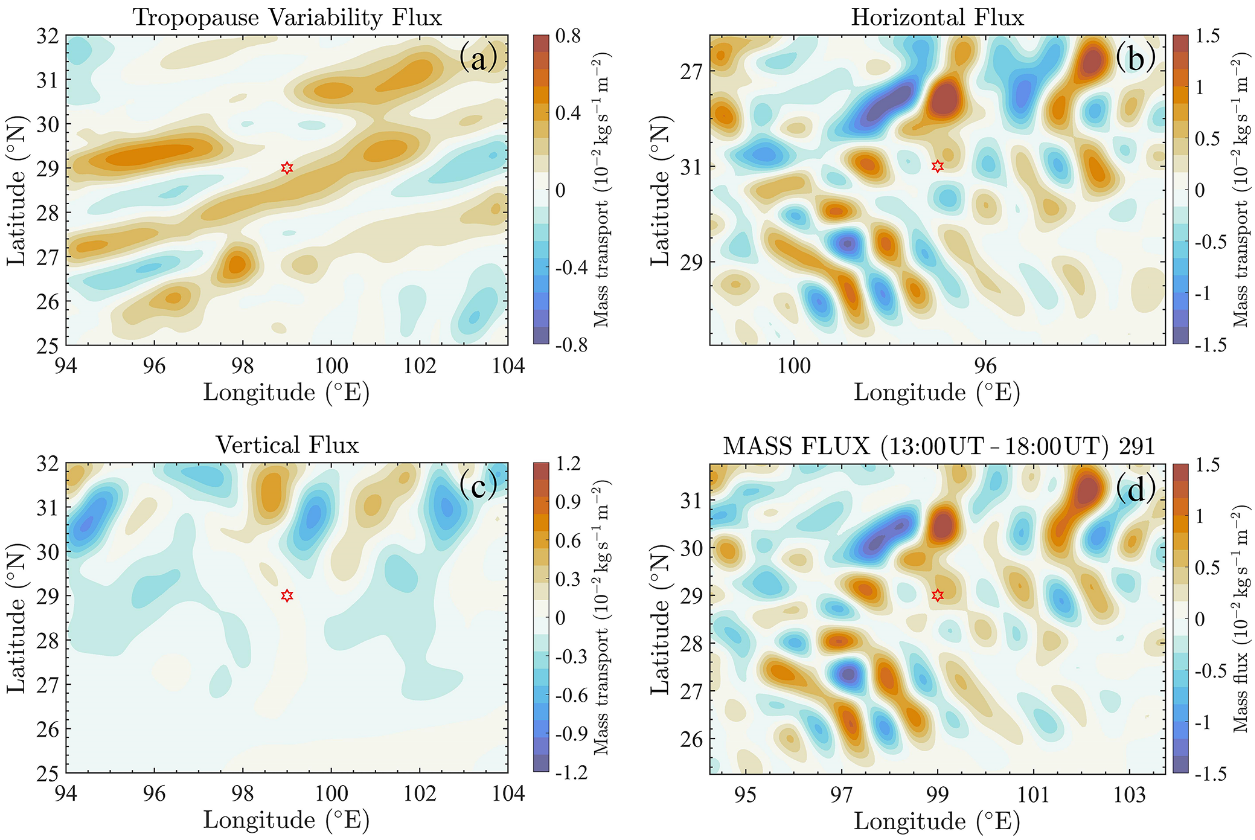

Figure 9. Spatial distributions of the cross-tropopause mass-flux components diagnosed using Wei's formulation and ERA5 meteorological fields during 13:00–18:00 on 18 October 2017. Each panel shows the 6 h mean of the instantaneous mass flux: **(a)** transport contribution from tropopause motion; **(b)** horizontal transport term; **(c)** vertical transport term; **(d)** total cross-tropopause mass flux. The red asterisk marks the location of the USTC Ozone Lidar at Yangbajing (29° N, 99° E).

being replaced by a vertically uniform ozone concentration.

$$F_q = M_{\mathrm{up}} \frac{\int_{p_{\mathrm{tropopause}-3}}^{p_{\mathrm{tropopause}}} q(p)\mathrm{d}p}{\int_{p_{\mathrm{tropopause}-3}}^{p_{\mathrm{tropopause}}} \mathrm{d}p} + M_{\mathrm{down}} \frac{\int_{p_{\mathrm{tropopause}}}^{p_{\mathrm{tropopause}+3}} q(p)\mathrm{d}p}{\int_{p_{\mathrm{tropopause}}}^{p_{\mathrm{tropopause}+3}} \mathrm{d}p}. \quad (3)$$

In the equation, $q(p)$ represents the uniform mixing ratio of ozone at pressure p, M_{up} denotes the upward flux of substances through the tropopause, and M_{down} denotes the downward flux of substances. Positive and negative values indicate locations above and below the tropopause, respectively. Thus, the observed vertical variation of ozone within the 3 km layers above and below the tropopause is retained in the integration rather than assuming a vertically uniform ozone abundance. The two integral terms represent the pressure-weighted layer-mean ozone mixing ratios on the tropospheric and stratospheric sides of the tropopause, respectively.

The instantaneous cross-tropopause ozone flux diagnosed at the Yangbajing lidar site for 18–19 October 2017 is shown in Fig. 11. A clear STE-related ozone descent signal is evident from 13:00 UT on 18 October to 12:00 UT on 19 October, manifested as a positive ozone flux from the stratosphere to the troposphere. In contrast, Aura satellite sampling near the site is temporally sparse. MLS typically overpasses the vicinity of Yangbajing only twice per day, whereas OMI provides at most one pass per day, which largely explains the relatively low temporal resolution of the satellite products. For 18–19 October, MLS provides three nearby footprints at (29.66° N, 98.27° E), (25.22° N, 105.20° E), and (29.66° N, 95.52° E) (red hexagons in Fig. 11). The first and third footprints are closest to the Yangbajing site, and the ozone fluxes inferred from MLS there agree well with the ERA5 estimates. By contrast, the second footprint is displaced substantially in longitude and lies outside the Tibetan Plateau, and its inferred ozone flux deviates more strongly from both the ERA5 and lidar results. Overall, the ozone flux derived from the USTC Ozone Lidar measured profiles is broadly consistent with the ERA5-driven ozone flux. More specifically, on 18 October, the lidar observations mainly capture the intensification phase and yield slightly larger diagnosed fluxes than

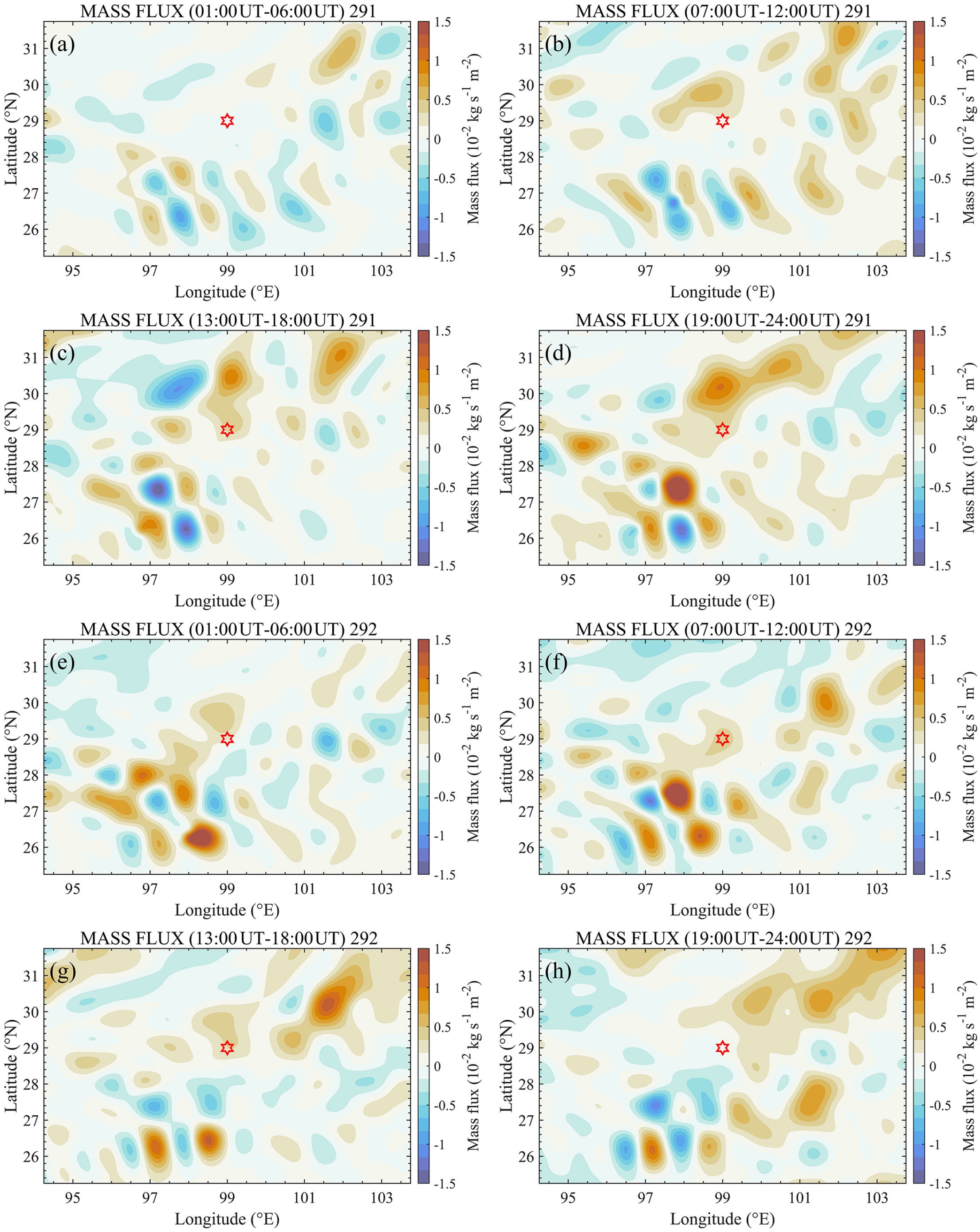

Figure 10. Spatiotemporal evolution of the cross-tropopause mass flux during 18–19 October 2017, diagnosed using Wei's formulation and ERA5 meteorological fields. Each panel shows the 6 h mean of the instantaneous cross-tropopause mass flux for the corresponding time interval. The red asterisk marks the location of the USTC Ozone Lidar at Yangbajing (29° N, 99° E).

ERA5, whereas on 19 October, during the recovery phase, the two estimates closely agree.

In this study, we present an initial detection and analysis of a stratosphere–troposphere exchange (STE) event captured by ozone lidar observations. The ozone flux associated with stratosphere-to-troposphere transport derived from the USTC Ozone Lidar exhibits an instantaneous peak of approximately $3–4 \times 10^{-10}$ kg s^{-1} m^{-2}, slightly exceeding the corresponding estimate derived from ERA5 for the same period. Despite this difference, the overall agreement between the lidar-derived and ERA5-derived ozone fluxes supports the robustness of the flux-calculation framework. Although ozone lidar

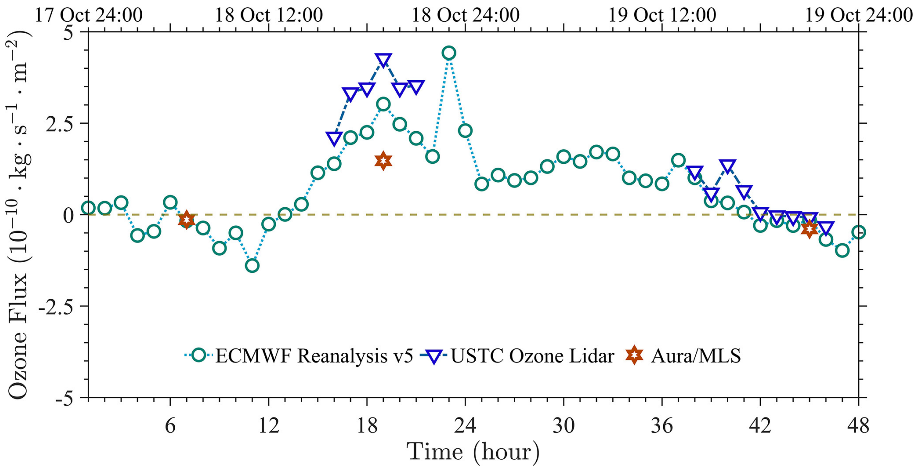

Figure 11. Instantaneous cross-tropopause ozone flux during 18–19 October 2017.

provides ozone concentration measurements with high spatial and temporal resolution, the lack of time-continuous in situ wind observations necessitates the use of ERA5 wind fields at 1 h resolution in the flux diagnosis. Despite this limitation, our analysis demonstrates that ozone-profiling lidar can not only resolve the fine vertical structure of ozone but also, when combined with wind information, enable quantitative observation and flux estimation of STE-related downward ozone transport, thereby broadening the potential of lidar for studies of coupled atmospheric composition and dynamics.

4 Conclusion

This study uses vertical profiles of ozone density observed by our mobile differential absorption ozone lidar (USTC Ozone Lidar) located at Yangbajing, Tibet (29° N, 99° E). The system provides synchronous observations of tropospheric and stratospheric ozone over 5–50 km, offering high-spatiotemporal-resolution profile evidence for STE studies over the Tibetan Plateau. By combining 30 min signal accumulation with a moving-window procedure, the dataset maintains a high effective temporal sampling while ensuring an adequate signal-to-noise ratio and showing strong consistency with ECMWF Reanalysis v5 (ERA5) and independent satellite observations.

To corroborate the STE-related ozone descent event identified from the lidar retrievals on 18–19 October 2017, ERA5 global reanalysis was used as an independent constraint. Near the tropopause, the ozone number densities observed by the USTC Ozone Lidar agree closely with ERA5 in both magnitude and temporal evolution, lending confidence to the event identification and the subsequent quantitative diagnostics. For the rapid ozone descent features resolved by the lidar, temperature profiles retrieved from the 387 nm N_2 vibrational Raman return reveal a strong correspondence with temperature fluctuations in the tropopause region. In six of the seven identified descent episodes, the associated temperature gradient exceeds $8\,K\,km^{-1}$, and even in the remaining case the gradient still reaches $4.2\,K\,km^{-1}$. These results represent the first detection of such rapid descent features by the USTC Ozone Lidar, together with the first identification of their close relationship to tropopause-region temperature variability using lidar-derived temperature profiles. In addition, the ozone descent observed at Yangbajing generally lags the broader descent over the study region (25–32° N, 94–104° E). The spatial distribution of cross-tropopause mass flux was diagnosed using the Wei formulation, with the PV-threshold sensitivity analysis supporting 3 PVU as a physically reasonable dynamical tropopause threshold for this event. The diagnosed flux fields further suggest that this STE event was closely linked to tropopause folding within the study region (25–32° N, 94–104° E), with the ozone variability observed at the lidar site modulated by gravity waves associated with the evolving fold.

Building on the mass-flux diagnosis, we directly incorporate lidar-measured ozone profiles into a cross-tropopause ozone-flux framework to quantify the downward ozone flux and validate the estimates against ERA5-driven results and Aura/MLS observations. The results show that the instantaneous peak ozone flux associated with stratosphere-to-troposphere transport, measured by the USTC Ozone Lidar, is approximately $3–4\times10^{-10}\,kg\,s^{-1}\,m^{-2}$, slightly exceeding the corresponding ERA5-derived estimate for the same period. Because time-continuous in situ wind measurements are not available, the flux calculation still relies on ERA5 wind fields. Even with this limitation, the results demonstrate that ozone-profiling lidar can resolve fine-scale vertical ozone structures and, when combined with wind information and dynamical diagnostics, contribute to the quantitative assessment of STE-related ozone transport and cross-tropopause ozone fluxes. Looking ahead, we will further develop and deploy a high-accuracy, high-temporal-resolution vertical wind profiling lidar to strengthen observations of coupled composition-dynamics processes over Tibet and to extend the utility of ozone lidar in such studies.

Code and data availability. The lidar data underlying this study were acquired with the USTC Ozone Lidar, which is operated as part of a large-scale scientific research infrastructure of the Chinese Academy of Sciences. Under the institutional data-management policy governing this research infrastructure, external release of the lidar data requires institutional review and authorization. Therefore, these data cannot currently be deposited in a public repository but are available from the corresponding author upon reasonable request, subject to institutional approval. The analysis code used in this study is available from the corresponding author upon reasonable request.

Author contributions. Conceptualization, R.D. and X.F.; methodology, R.D.; validation, R.D., C.Y. and X.F.; formal analysis, C.Y.; writing-original draft preparation, R.D.; writing-review and editing, T.L. and X.F.; funding acquisition, T.L. and X.F.; All authors have read and agreed to the published version of the manuscript.

Competing interests. The contact author has declared that none of the authors has any competing interests.

Disclaimer. Publisher's note: Copernicus Publications remains neutral with regard to jurisdictional claims made in the text, published maps, institutional affiliations, or any other geographical representation in this paper. The authors bear the ultimate responsibility for providing appropriate place names. Views expressed in the text are those of the authors and do not necessarily reflect the views of the publisher.

Acknowledgements. We thank all other members in team for their contribution to the system installation. We also thank Dan Chen from the School of Atmospheric Sciences, Nanjing University of Information Science and Technology; Yun Bi from the School of Earth and Space Sciences, University of Science and Technology of China; Xianhang Chen, a former master's student in our research group; and the other colleagues and students who provided valuable assistance. We acknowledge for the data resources from "National Space Science Data Center, National Science & Technology Infrastructure of China. (https://www.nssdc.ac.cn, last access: 27 July 2026)". We acknowledge for the data provider University of Science and Technology of China. The Aura/MLS data is downloaded from https://search.earthdata.nasa.gov/search (last access: 27 July 2026).

Financial support. This research has been supported by the National Natural Science Foundation of China (grant nos. 42130203 and 41974177); National Key Research and Development Program of China (grant no. 2022YFF0503703); B-type Strategic Priority Program of the Chinese Academy of Sciences (grant no. XDB41000000).

Review statement. This paper was edited by Bernd Funke and reviewed by three anonymous referees.

References

Ancellet, G., Pelon, J., Beekmann, M., Papayannis, A., and Mégie, G.: Ground-based lidar studies of ozone exchanges between the stratosphere and the troposphere, J. Geophys. Res.-Atmos., 96, 22401–22421, https://doi.org/10.1029/91jd02385, 1991.

Baray, J.-L., Courcoux, Y., Keckhut, P., Portafaix, T., Tulet, P., Cammas, J.-P., Hauchecorne, A., Godin Beekmann, S., De Mazière, M., Hermans, C., Desmet, F., Sellegri, K., Colomb, A., Ramonet, M., Sciare, J., Vuillemin, C., Hoareau, C., Dionisi, D., Duflot, V., Vérèmes, H., Porteneuve, J., Gabarrot, F., Gaudo, T., Metzger, J.-M., Payen, G., Leclair de Bellevue, J., Barthe, C., Posny, F., Ricaud, P., Abchiche, A., and Delmas, R.: Maïdo observatory: a new high-altitude station facility at Reunion Island (21° S, 55° E) for long-term atmospheric remote sensing and in situ measurements, Atmos. Meas. Tech., 6, 2865–2877, https://doi.org/10.5194/amt-6-2865-2013, 2013.

Bertin, F., Campistron, B., Caccia, J. L., and Wilson, R.: Mixing processes in a tropopause folding observed by a network of ST radar and lidar, Ann. Geophys., 19, 953–963, https://doi.org/10.5194/angeo-19-953-2001, 2001.

Boggess, A. and Narcowich, F. J.: A first course in wavelets with Fourier analysis, 2nd edn., John Wiley and Sons, ISBN 978-0-470-43117-7, 2009.

Browell, E. V., Ismail, S., and Shipley, S. T.: Ultraviolet DIAL measurements of O_3 profiles in regions of spatially inhomogeneous aerosols, Appl. Optics, 24, 2827–2836, https://doi.org/10.1364/ao.24.002827, 1985.

Chen, B., Xu, X.-D., Bian, J.-C., and Shi, X.-H.: Irreversible stratosphere-troposphere mass exchange characteristics over the Asian summer monsoon region, Chinese J. Geophys.-Ch., 53, 1050–1059, https://doi.org/10.3969/j.issn.0001-5733.2010.05.005, 2010 (in Chinese).

Chen, C., Tian, W. S., Tian, H. Y., Huo, Y. F., Shu, J. C., Xie, F., Xuan, Y. J., and Wan, X. W.: Vertical distribution of ozone and stratosphere-troposphere exchanges on the northeastern side of Tibetan Plateau, Plateau Meteorol., 31, 295–303, 2012 (in Chinese).

Chen, H., Bian, J., and Lü, D.: Advances and prospects in the study of stratosphere-troposphere exchange, Chin. J. Atmos. Sci., 30, 813–820, https://doi.org/10.3878/j.issn.1006-9895.2006.05.10, 2006 (in Chinese).

Cho, J. Y. N., Newell, R. E., Bui, T. P., Browell, E. V., Fenn, M. A., Mahoney, M. J., Gregory, G. L., Sachse, G. W., Vay, S. A., Kucsera, T. L., and Thompson, A. M.: Observations of convective and dynamical instabilities in tropopause folds and their contribution to stratosphere-troposphere exchange, J. Geophys. Res.-Atmos., 104, 21549–21568, https://doi.org/10.1029/1999jd900430, 1999.

Cui, H., Zhao, C., Qin, Y., Zheng, X., Zheng, Y., Chan, C. Y., and Chan, L. Y.: An estimation of ozone flux in a stratosphere-troposphere exchange event, Chinese Sci. Bull., 49, 167–174, 2004.

Duan, A. M. and Wu, G. X.: Role of the Tibetan Plateau thermal forcing in the summer climate patterns over subtropical Asia, Clim. Dynam., 24, 793–807, https://doi.org/10.1007/s00382-004-0488-8, 2005.

Duchnowski, R. and Wyszkowska, P.: Laser scanning data processed using Msplit estimation and sliding window algorithm, Rep. Geod. Geoinf., 120, 67–74, https://doi.org/10.2478/rgg-2025-0017, 2025.

Eisele, H., Scheel, H. E., Sladkovic, R., and Trickl, T.: High-resolution lidar measurements of stratosphere–troposphere exchange, J. Atmos. Sci., 56, 319–330, https://doi.org/10.1175/1520-0469(1999)056<0319:hrlmos>2.0.co;2, 1999.

Fang, H. and Huang, D.: Lidar signal de-noising based on wavelet trimmed thresholding technique, Chin. Opt. Lett., 2, 1–3, 2004.

Fang, X., Li, T., Ban, C., Wu, Z., Li, J., Li, F., Cen, Y., and Tian, B.: A mobile differential absorption lidar for simultaneous observations of tropospheric and stratospheric ozone over Tibet, Opt. Express, 27, 4126–4139, https://doi.org/10.1364/oe.27.004126, 2019.

Gettelman, A., Salby, M. L., and Sassi, F.: Distribution and influence of convection in the tropical tropopause region, J. Geophys. Res.-Atmos., 107, 4080, https://doi.org/10.1029/2001jd001048, 2002.

Gimmestad, G. G.: Differential-Absorption Lidar for Ozone and Industrial Emissions, in: Lidar: Range-Resolved Optical Remote Sensing of the Atmosphere, Springer Series in Optical Sciences, 102, edited by: Weitkamp, C., Springer, 187–212, https://doi.org/10.1007/0-387-25101-4_7, 2005.

Godin-Beekmann, S., Porteneuve, J., and Garnier, A.: Systematic DIAL lidar monitoring of the stratospheric ozone vertical distribution at Observatoire de Haute-Provence (43.92° N, 5.71° E), J. Environ. Monitor., 5, 57–67, https://doi.org/10.1039/b205880d, 2003.

Hansen, G., Bramstedt, K., Rozanov, V., Weber, M., and Burrows, J. P.: Validation of GOME ozone profiles by means of the ALOMAR ozone lidar, Ann. Geophys., 21, 1879–1886, https://doi.org/10.5194/angeo-21-1879-2003, 2003.

Hersbach, H., Bell, B., Berrisford, P., Hirahara, S., Horányi, A., Muñoz-Sabater, J., Nicolas, J., Peubey, C., Radu, R., Schepers, D., Simmons, A., Soci, C., Abdalla, S., Abellan, X., Balsamo, G., Bechtold, P., Biavati, G., Bidlot, J., Bonavita, M., De Chiara, G., Dahlgren, P., Dee, D., Diamantakis, M., Dragani, R., Flemming, J., Forbes, R., Fuentes, M., Geer, A., Haimberger, L., Healy, S., Hogan, R. J., Hólm, E., Janisková, M., Keeley, S., Laloyaux, P., Lopez, P., Lupu, C., Radnoti, G., de Rosnay, P., Rozum, I., Vamborg, F., Villaume, S., and Thépaut, J.-N.: The ERA5 global reanalysis, Q. J. Roy. Meteor. Soc., 146, 1999–2049, https://doi.org/10.1002/qj.3803, 2020.

Holton, J. R., Haynes, P. H., McIntyre, M. E., Douglass, A. R., Rood, R. B., and Pfister, L.: Stratosphere-troposphere exchange, Rev. Geophys., 33, 403–439, https://doi.org/10.1029/95rg02097, 1995.

Kourtidis, K., Zerefos, C., Rapsomanikis, S., Simeonov, V., Balis, D., Perros, P. E., Thompson, A. M., Witte, J., Calpini, B., Sharobiem, W. M., Papayannis, A., Mihalopoulos, N., and Drakou, R.: Regional levels of ozone in the troposphere over eastern Mediterranean, J. Geophys. Res.-Atmos., 107, 8140, https://doi.org/10.1029/2000jd000140, 2002.

Kovalev, V. A. and Bristow, M. P.: Compensational three-wavelength differential-absorption lidar technique for reducing the influence of differential scattering on ozone-concentration measurements, Appl. Optics, 35, 4790–4797, https://doi.org/10.1364/ao.35.004790, 1996.

Kovalev, V. A. and Eichinger, W. E.: Elastic lidar: theory, practice, and analysis methods, John Wiley and Sons, https://doi.org/10.1002/0471643173, 2004.

Kuang, S., Newchurch, M. J., Burris, J., Wang, L., Knupp, K., and Huang, G.: Stratosphere-to-troposphere transport revealed by ground-based lidar and ozonesonde at a midlatitude site, J. Geophys. Res.-Atmos., 117, D18305, https://doi.org/10.1029/2012jd017695, 2012.

Langford, A. O., Masters, C. D., Proffitt, M. H., Hsie, E.-Y., and Tuck, A. F.: Ozone measurements in a tropopause fold associated with a cut-off low system, Geophys. Res. Lett., 23, 2501–2504, https://doi.org/10.1029/96gl02227, 1996.

Lelieveld, J. and Dentener, F. J.: What controls tropospheric ozone?, J. Geophys. Res.-Atmos., 105, 3531–3551, https://doi.org/10.1029/1999jd901011, 2000.

Liu, X., Bhartia, P. K., Chance, K., Spurr, R. J. D., and Kurosu, T. P.: Ozone profile retrievals from the Ozone Monitoring Instrument, Atmos. Chem. Phys., 10, 2521–2537, https://doi.org/10.5194/acp-10-2521-2010, 2010.

McDermid, I. S., Haner, D. A., Kleiman, M. M., Walsh, T. D., and White, M. L.: Differential absorption lidar systems for tropospheric and stratospheric ozone measurements, Opt. Eng., 30, 22–30, https://doi.org/10.1117/12.55768, 1991.

McGee, T. J., Gross, M., Ferrare, R., Heaps, W., and Singh, U.: Raman DIAL measurements of stratospheric ozone in the presence of volcanic aerosols, Geophys. Res. Lett., 20, 955–958, https://doi.org/10.1029/93gl00751, 1993.

McIntyre, M. E. and Palmer, T. N.: Breaking planetary waves in the stratosphere, Nature, 305, 593–600, https://doi.org/10.1038/305593a0, 1983.

McIntyre, M. E. and Palmer, T. N.: The “surf zone” in the stratosphere, J. Atmos. Terr. Phys., 46, 825–849, https://doi.org/10.1016/0021-9169(84)90063-1, 1984.

Olsen, M. A., Schoeberl, M. R., and Douglass, A. R.: Stratosphere-troposphere exchange of mass and ozone, J. Geophys. Res.-Atmos., 109, D24114, https://doi.org/10.1029/2004jd005186, 2004.

Papayannis, A. D., Porteneuve, J., Balis, D., Zerefos, C., and Galani, E.: Design of a new DIAL system for tropospheric and lower stratospheric ozone monitoring in Northern Greece, Phys. Chem. Earth Pt. C, 24, 439–442, https://doi.org/10.1016/s1464-1917(99)00068-9, 1999.

Randel, W. J. and Park, M.: Deep convective influence on the Asian summer monsoon anticyclone and associated tracer variability observed with Atmospheric Infrared Sounder (AIRS), J. Geophys. Res.-Atmos., 111, D12314, https://doi.org/10.1029/2005jd006490, 2006.

Randel, W. J., Park, M., Emmons, L., Kinnison, D., Bernath, P., Walker, K. A., Boone, C., and Pumphrey, H.: Asian monsoon transport of pollution to the stratosphere, Science, 328, 611–613, https://doi.org/10.1126/science.1182274, 2010.

Reiter, E. R.: Stratospheric-tropospheric exchange processes, Rev. Geophys., 13, 459–474, https://doi.org/10.1029/rg013i004p00459, 1975.

Schoeberl, M. R., Douglass, A. R., Hilsenrath, E., Bhartia, P. K., Beer, R., Waters, J. W., Gunson, M. R., Froidevaux, L., Gille, J. C., Barnett, J. J., Levelt, P. F., and DeCola, P.: Overview of the EOS Aura mission, IEEE T. Geosci. Remote, 44, 1066–1074, https://doi.org/10.1109/tgrs.2005.861950, 2006.

Shangguan, M., Wang, W., and Jin, S.: Variability of temperature and ozone in the upper troposphere and lower stratosphere from multi-satellite observations and reanalysis data, Atmos. Chem. Phys., 19, 6659–6679, https://doi.org/10.5194/acp-19-6659-2019, 2019.

Škerlak, B., Sprenger, M., and Wernli, H.: A global climatology of stratosphere–troposphere exchange using the ERA-Interim data set from 1979 to 2011, Atmos. Chem. Phys., 14, 913–937, https://doi.org/10.5194/acp-14-913-2014, 2014.

Škerlak, B., Sprenger, M., Pfahl, S., Tyrlis, E., and Wernli, H.: Tropopause folds in ERA-Interim: Global climatology and relation to extreme weather events, J. Geophys. Res.-Atmos., 120, 4860–4877, https://doi.org/10.1002/2014jd022787, 2015.

Sprenger, M., Croci Maspoli, M., and Wernli, H.: Tropopause folds and cross-tropopause exchange: A global investigation based upon ECMWF analyses for the time period March 2000 to February 2001, J. Geophys. Res.-Atmos., 108, 8518, https://doi.org/10.1029/2002jd002587, 2003.

Standard, U.S.: Atmosphere, National Oceanic and Atmospheric Administration, 1976.

Stohl, A., Bonasoni, P., Cristofanelli, P., Collins, W., Feichter, J., Frank, A., Forster, C., Gerasopoulos, E., Gäggeler, H., James, P., Kentarchos, T., Kromp-Kolb, H., Krüger, B., Land, C., Meloen, J., Papayannis, A., Priller, A., Seibert, P., Sprenger, M., Roelofs, G. J., Scheel, H. E., Schnabel, C., Siegmund, P., Tobler, L., Trickl, T., Wernli, H., Wirth, V., Zanis, P., and Zerefos, C.: Stratosphere-troposphere exchange: A review, and what we have learned from STACCATO, J. Geophys. Res.-Atmos., 108, 8516, https://doi.org/10.1029/2002jd002490, 2003.

Tian, W., Chipperfield, M., and Huang, Q.: Effects of the Tibetan Plateau on total column ozone distribution, Tellus B, 60, 622–635, https://doi.org/10.1111/j.1600-0889.2008.00338.x, 2008.

Trickl, T., Vogelmann, H., Ries, L., and Sprenger, M.: Very high stratospheric influence observed in the free troposphere over the northern Alps – just a local phenomenon?, Atmos. Chem. Phys., 20, 243–266, https://doi.org/10.5194/acp-20-243-2020, 2020.

Waters, J. W., Froidevaux, L., Harwood, R. S., Jarnot, R. F., Pickett, H. M., Read, W. G., Siegel, P. H., Cofield, R. E., Filipiak, M. J., Flower, D. A., Holden, J. R., Lau, G. K., Livesey, N. J., Manney, G. L., Pumphrey, H. C., Santee, M. L., Wu, D. L., Cuddy, D. T., Lay, R. R., Loo, M. S., Perun, V. S., Schwartz, M. J., Stek, P. C., Thurstans, R. P., Boyles, M. A., Chandra, K. M., Chavez, M. C., Chen, G.-S., Chudasama, B. V., Dodge, R., Fuller, R. A., Girard, M. A., Jiang, J. H., Jiang, Y., Knosp, B. W., LaBelle, R. C., Lam, J. C., Lee, K. A., Miller, D., Oswald, J. E., Patel, N. C., Pukala, D. M., Quintero, O., Scaff, D. M., Van Snyder, W., Tope, M. C., Wagner, P. A., and Walch, M. J.: The Earth observing system microwave limb sounder (EOS MLS) on the Aura satellite, IEEE T. Geosci. Remote, 44, 1075–1092, https://doi.org/10.1109/tgrs.2006.873771, 2006.

Wei, M. Y.: A new formulation of the exchange of mass and trace constituents between the stratosphere and troposphere, J. Atmos. Sci., 44, 3079–3086, https://doi.org/10.1175/1520-0469(1987)044<3079:anfote>2.0.co;2, 1987.

Wernli, H. and Bourqui, M.: A Lagrangian "1-year climatology" of (deep) cross-tropopause exchange in the extratropical Northern Hemisphere, J. Geophys. Res.-Atmos., 107, 4021, https://doi.org/10.1029/2001jd000812, 2002.

Wirth, V.: Comments on "A New Formulation of the Exchange of Mass and Trace Constituents between the Stratosphere and Troposphere", J. Atmos. Sci., 52, 2491–2493, https://doi.org/10.1175/1520-0469(1995)052<2491:confot>2.0.co;2, 1995.

Wirth, V. and Egger, J.: Diagnosing extratropical synoptic-scale stratosphere-troposphere exchange: A case study, Q. J. Roy. Meteor. Soc., 125, 635–655, https://doi.org/10.1002/qj.49712555413, 1999.

Yang, J. and Lü, D.: A simulation study of stratosphere-troposphere exchange due to cut-off-low over eastern Asia, Chin. J. Atmos. Sci., 27, 1031–1044, https://doi.org/10.3878/j.issn.1006-9895.2003.06.07, 2003 (in Chinese).

Yang, J. and Lü, D.: Diagnosed seasonal variation of stratosphere-troposphere exchange in the Northern Hemisphere by 2000 data, Chin. J. Atmos. Sci., 28, 294–300, https://doi.org/10.3878/j.issn.1006-9895.2004.02.12, 2004 (in Chinese).

Yin, S. and Wang, W.: Denoising lidar signal by combining wavelet improved threshold with wavelet domain spatial filtering, Chin. Opt. Lett., 4, 694–696, 2006.

Zhang, M., Tian, W., Chen, L., and Lü, D.: Cross-tropopause mass exchange associated with a tropopause fold event over the northeastern Tibetan Plateau, Adv. Atmos. Sci., 27, 1344–1360, https://doi.org/10.1007/s00376-010-9129-9, 2010.

Zhang, Y., Huang, Q., Guo, K., Wang, M., Liao, H., Chou, Y., and He, X.: Tropopause folds over the Tibetan Plateau and their impact on water vapor in the upper troposphere-lower stratosphere, Clim. Dynam., 62, 1423–1437, https://doi.org/10.1007/s00382-023-06978-2, 2024.

Zhou, S. and Zhang, R.: Decadal variations of temperature and geopotential height over the Tibetan Plateau and their relations with Tibet ozone depletion, Geophys. Res. Lett., 32, L18705, https://doi.org/10.1029/2005gl023496, 2005.